ELSEVIER

Contents lists available at ScienceDirect

Computers and Geotechnics

journal homepage: www.elsevier.com/locate/compgeo





Coupling irregular particles and fluid: Complex dynamics of granular flows

Xiaoming Zhang, Pejman Tahmasebi ^{*}

College of Engineering and Applied Science, University of Wyoming, Laramie, WY 82071, USA

ABSTRACT

Granular materials are often encountered in nature, but the effect of their morphological properties is poorly understood when they are accompanied by fluid. This set of complexity brings the inertial, viscous, frictional, and elastic forces together whose connections remain debated. We report a novel coupled framework to study the effect of particle morphology on the dynamics of granular particles. The mechanical behavior is modeled by a new micro-mechanical model and is found to be greatly impeded by the morphology of particles. The movement difference caused by the particle shape is greatly alleviated by the presence of fluid. Our findings are demonstrated using a collapse process and we found that the dislocation is both hindered and enhanced by the viscous and lubrication effects of fluid, respectively. The results show that the effect of the fluid lubrication becomes dominant compared to the fluid viscous effect when particles become more irregular.

1. Introduction

The dynamic behavior of granular systems is often observed in nature, such as landslides, collapse, debris flows, and solid deformation in porous media, as well as in modern chemical industries, pharmaceutics, mining, food processing, and cosmetics (Zhao and Shan, 2013; Zhu et al., 2008, 2007). Understanding the fundamental mechanisms governing the flow or deformation of granular systems is of great importance to predict natural disasters or optimize the design for relevant industrial processes. The macroscopic behavior of granular systems is the result of microscopic interactions, which exist between particle-particle, particle-wall as well as fluid-particle in a wet environment. Research on the microscopic mechanism of granular systems has been widely developed. Particularly, the Discrete Element Method (DEM) introduced by Cundall and Strack has been extensively cultivated to simulate various particulate movements (Cundall and Strack, 1979). In principle, the DEM adopts a soft-sphere model, where particles are allowed to deform or overlap, to calculate elastic or frictional forces between particles. In this method, the trajectory of each particle is tracked separately, and their translational and rotational movements are calculated by Newton's equations of motion.

However, it has been proven, both experimentally and computationally, that particles' morphology greatly determines macroscopic properties of granular particles, such as strength, permeability, energy dissipation, packing, bulk density, porosity, shear strength, cohesion, energy transfer, stress distribution, and so on (Anthony and Marone, 2005; Cho et al., 2006; Jerves et al., 2016; Karimpouli and Tahmasebi, 2016; Mair et al., 2002; Murphy et al., 2019; Saadatfar et al., 2012,

2010). Many representation techniques have been studied to depict the irregular shapes of natural particles. Among these techniques, clustering/clumping and polyhedra are widely used to capture the complex morphologies (Adepu et al., 2020; Chen et al., 2017; Ferellec and McDowell, 2010; Garcia et al., 2009; Peña et al., 2008; Seyedi Hosseininia and Mirghasemi, 2006). Both techniques are, however, rather crude and fail to accurately describe the real morphology of particles. More advanced methods to capture particle morphology are based on Xray computed tomographic (XRCT) image data (Desrues et al., 2010). One of the initial methods in this group was based on the "potential particle" through which the complex particles can be described for DEM (Boon et al., 2012; Houlsby, 2009). This method represents the particle by a function using local coordinates f(x,y) = 0 in which the inside, surface, and outside of particles can be described by f < 0, f = 0, and f > 0, respectively. The methods developed after this idea all try to make the representation of f more accurate. For example, non-uniform rational basis-splines or level-set are two of such methods (Houlsby, 2009; Kawamoto et al., 2016; Lim and Andrade, 2014), which both aim to represent the shape of particles more efficiently. Such techniques can represent particle's morphology and simulate the mechanical behaviors, but they are computationally prohibitive. Aside from such issues, there exist no method that can take the presence of fluid into account. Here, thus, we propose to take advantage of an enhanced distance transform (EDT) method as an efficient and accurate method to improve the computational efficiency and capture the particle's morphology (Bailey, 2005; Felzenszwalb and Huttenlocher, 2012; Huang and Mitchell, 1994). We call this new technique as image-based DEM (iDEM), which is applied for simulating the dynamics of particles. Compared with pure

E-mail address: ptahmase@uwyo.edu (P. Tahmasebi).

^{*} Corresponding author.

particle flow, fluid-particle flow, in which the fluid phase and solid phase affect the motion of each other, is more complicated. Different simulation methods have been developed for the fluid-particle flow. Robinson and Ramaioli et al. (Robinson et al., 2014) presented a meshless simulation method for multiphase fluid-particle flow by coupling Smoothed Particle Hydrodynamics (SPH) for the fluid and DEM for the solid phase. They successfully reproduced the expected behavior in 3D sedimentation cases with single and multiple particles. This method may not capture the fine-scale phenomenon, but it is well suited for systems for large deformations. Cheng and Luding et al. (Cheng et al., 2019) simulated the wave propagation in saturated poroelastic granular crystals by a hydro-micromechanical model in which the pore fluid was resolved by the lattice Boltzmann method (LBM) and the particle motion was simulated by DEM. LBM can reproduce the fine-scale flow behaviors but it can be computationally expensive for large systems. Along with such modeling, coupled computational fluid dynamics - discrete element method (CFD-DEM) has become an increasingly popular Eulerian-Lagrangian technique (Tahmasebi and Kamrava, 2019; Tomac and Gutierrez, 2014, 2013; Zhang and Tahmasebi, 2019, 2018; Zhu et al., 2008, 2007). In these methods, DEM is in charge of the motion of individual particles while the flow behavior of fluid is calculated by the CFD (Hoomans et al., 1996; Tsuji et al., 1992; Xu and Yu, 1997), which can be computationally more feasible. These methods have been, however, limited to spherical or well-defined particles. Only limited development on the non-spherical CFD-DEM have been made, such as cylinder-shaped particles and super-quadric particles (Hilton et al., 2010; Ren et al., 2012; Zhong et al., 2009). Zhong et al. summarized the theoretical developments and applications of DEM/CFD-DEM simulation of nonspherical particles (Zhong et al., 2016). In this paper, we will simulate both the motion of fully irregular particles and fluid flow by a coupled CFD-iDEM through which the effect of fluid flow in systems with angular particles is taken into account in a numerically efficient method.

In this paper, we first generate various granular packings to represent different morphologies, which will then be simulated for both dry (without fluid) and wet cases (with fluid). Our collapse results demonstrate that both the particle morphology and fluid have an important effect on the runout and final configuration of collapse. With the consideration of irregular shapes of particles and fluid, this work sets the foundation for granular flows in nature, such as landslides, avalanches, and debris flows, hence providing a unique solution that can be used in other fields related to granular particles.

2. Model specification

2.1. Distance transform

Distance transform is one popular image analysis technique to label the pixel of the foreground in a binary image with the minimum distance value to the background pixels. Mathematically, the minimum distance for one object pixel is calculated by (Bailey, 2005):

$$D(p) = \min(\|p - q\|), \tag{1}$$

where ||p-q|| is a measure of the distance between one arbitrary object pixel p and one arbitrary background pixel q. There are several common measures, such as Euclidean distance metric, city block metric, and chessboard metric (Bailey, 2005). Here we adopt the Euclidean distance metric because it calculates the distance by imitating the real measurement for objects. In the Cartesian coordinates, the Euclidean distance is calculated by the following equation:

$$||p-q||_{L_2} = \sqrt{(x_p - x_q)^2 + (y_p - y_q)^2}.$$
 (2)

The distance computation is the essential part of the distance transform, which offers an excellent and efficient method in the context of representing complex particles. However, it should be noticed that distance transform only considers the distance values inside the particles, that is, the distance fields computed by distance transform are usually unsigned. To make the distance fields for particles being signed and smooth, we take some steps to achieve the requirements:

- 1. Using binary representation data of a particle, as shown in Fig. 1 (a). Here, white and black regions represent the particle and pore, respectively. This data is used to compute the negative distance values inside of the particle (Fig. 1(b)) and the positive distance values outside of the particle (Fig. 1(c)), and then to obtain the signed distance field of the particle (Fig. 1(d)) by combining the two previously computed distance fields
- 2. Applying Gaussian filtering on the signed distance field to compute the smoothed distance field (Buades et al., 2005; Gedraite and Hadad, 2011; Kong et al., 2013), and using trilinear interpolation to find the particle surface whose distance values are equal to zero, and discretizing the surface to nodes.

In this paper, we use a node-to-surface algorithm for the contact problem of nonconvex particles with multiple contact nodes, which is other discrete element models for non-spherical particles (Kawamoto et al., 2016; Laursen, 2013; Lim et al., 2014). It has been found that setting node-to-node spacing to be one-tenth of the diameter of a given particle is adequate to represent the particle morphology as more nodes make a negligible improvement on accuracy (Kawamoto et al., 2016). With the distance transform, 3D particles are represented in Fig. 2, which shows different morphologies for four random particles selected from the produced assemblies.

When one particle is characterized into the distance field, the positive, negative, and zero distance values represent the outside, inside, and surface of the particle, respectively. Then, the inertial properties, such as the mass, center of mass, and moment of inertia of a given particle, are the necessary attributes for accounting for the motion of the particle. These properties are calculated directly by employing the distance field of the particle (Kawamoto et al., 2016).

2.2. Particle motion

The kinematic behavior of individual particles is described by Newton's second law, which is the principle of DEM simulation:

$$m_p \frac{du_p}{dt} = m_p g + \sum_{N_p} F_{p,p} + \sum_{N_w} F_{w,p},$$
 (3)

where m_p , u_p are the mass and the velocity of one granular particle, respectively. $\sum_{N_p} F_{p,p}$ is the total particle–particle interactions exerted on the particle which is in contact with N_p other particles. $\sum_{N_w} F_{w,p}$ is the total wall-particle interactions exerted on the particle which is in contact with N_w walls.

Particle-particle interaction $F_{p,p}$ and wall-particle interaction F_{wp} are caused by the collision, which can be classified as contact force. In the DEM, the contact force is determined by the soft-sphere model (Cundall and Strack, 1979). In the soft-sphere model, elastic and frictional forces are calculated when contacts in particle–particle or wall-particle are detected. The motion of particles is then described by Newton's law of motion. Before illustrating the calculation of the contact force $F_{p,p}$ between two particles, we need to detect the contact status and overlapping/penetration value of the two particles. For the sake of simplicity, we use two-dimensional (2D) particles to illustrate this concept, as shown in Fig. 3. Noting that the proposed method has full applicability for 3D.

Here, we take particle a as the target object to illustrate the contact detection and overlap calculation with its surrounding particle b or particle c. Thus, the following steps are taken:

1. The distance values for all nodes on the surface of particle a, referring to the distance field of particle b, are computed by the trilinear interpolation. Considering node i with position x_i^a , its distance value

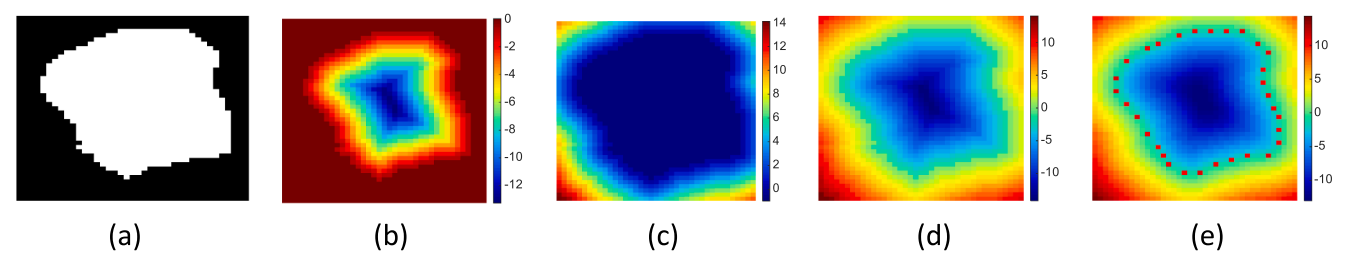


Fig. 1. 2D illustration for the characterization of a particle. (a) Binary representation for the particle. (b) Negative distance field inside the particle. (c) Positive distance field outside the particle. (d) Combined signed distance field. (e) Smoothed signed distance field with nodes in red seeded on the particle surface. (For interpretation of the references to colour in this figure legend, the reader is referred to the web version of this article.)

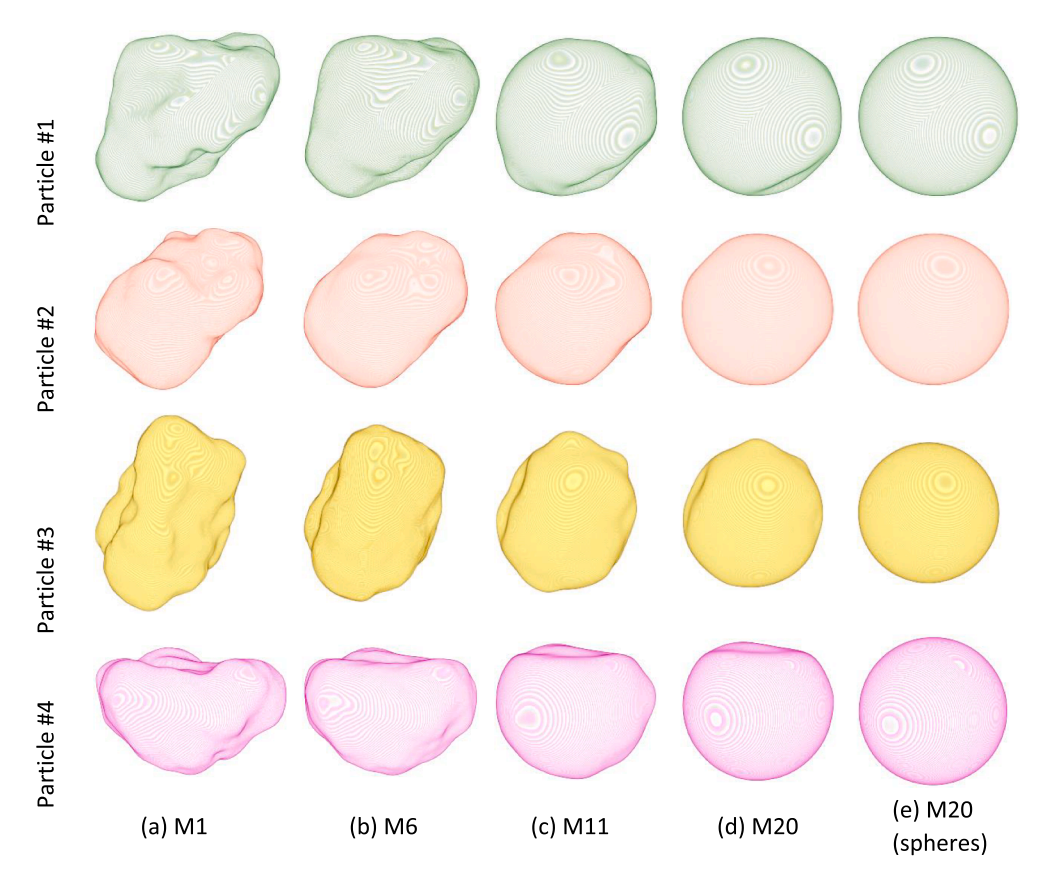


Fig. 2. Representation of various considered morphologies (shown by M) which are changing gradually from highly irregular (M1) to spherical particles (M20).

 $\Phi_b(\mathbf{x}_i^a)$ represents the distance from this node to the surface of particle b, and its distance gradient $\nabla\Phi_b(\mathbf{x}_i^a)$ represents the outward normal direction of particle b at node i.

2. If $\exists \Phi_b(x_i^a)$. < 0, that is, node i located inside of particle b, we consider the two particles to be in contact at the node i which is called contact node, as shown in Fig. 3. The overlap and contact normal vector at contact node i are calculated as:

$$d_i^{a,b} = \Phi_b(\mathbf{x}_i^a),\tag{4}$$

$$\boldsymbol{n}_{i}^{a,b} = -\frac{\nabla \Phi_{b}(\boldsymbol{x}_{i}^{a})}{\|\nabla \Phi_{b}(\boldsymbol{x}_{i}^{a})\|},\tag{5}$$

where $d_i^{a,b}$ and $n_i^{a,b}$ are the overlap and outward contact normal vector of particle a, respectively, at contact node i between particle a and particle b. The contact interaction between particle a and particle b is the sum of all the contact nodes existing between the two particles. The contact detection for particle a and its surrounding particle a has the same steps

as discussed above. Finally, the contact status with all the remaining surrounding particles of particle a is identified with the same method. Similarly, when particle b is considered as the target object, the contact status with all surrounding particles is also computed in the same way.

The normal contact force between particle a and particle b is calculated using a linear elastic model, which has the following form:

$$\boldsymbol{F}_{n,i}^{a} = -k_{n}d_{i}^{a,b}\boldsymbol{n}_{i}^{a,b},\tag{6}$$

where $F_{n,i}^a$ is the normal contact force exerted on particle a at contact node i. k_n is the normal elastic stiffness. By action and reaction, the normal contact force $F_{n,i}^b$ exerted on particle b at contact node i is calculated as:

$$\boldsymbol{F}_{n,i}^{b} = -\boldsymbol{F}_{n,i}^{a}.\tag{7}$$

The resulting moments $M_{n,i}^a$ and $M_{n,i}^b$ at contact node i are calculated using:

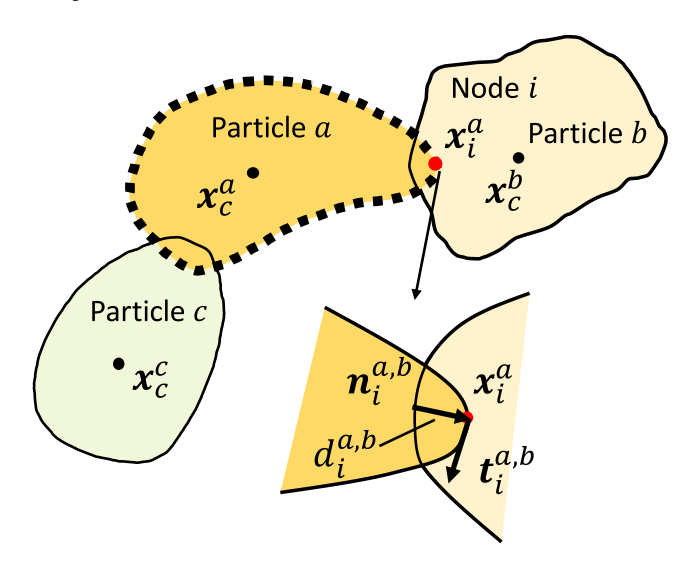


Fig. 3. Schematic of two contacting particles.

$$\mathbf{M}_{n,i}^{a} = \left(\mathbf{x}_{i}^{a} - \mathbf{x}_{c}^{a}\right) \times \mathbf{F}_{n,i}^{a},\tag{8a}$$

$$\mathbf{M}_{n,i}^b = (\mathbf{x}_i^a - \mathbf{x}_c^b) \times \mathbf{F}_{n,i}^b, \tag{8b}$$

where x_c^a and x_c^b are the centers of mass of particle a and particle b, respectively, and x_i^a is the position of the contact node i.

The tangential contact force between particle a and particle b is calculated using the Coulomb friction model similar to the friction model (Andrade et al., 2012). The relative velocity $v^{a,b}$ between particle a and particle b is given by:

$$\mathbf{v}^{a,b} = \mathbf{v}^a + \boldsymbol{\omega}^a \times (\mathbf{x}_i^a - \mathbf{x}_c^a) - \mathbf{v}^b - \boldsymbol{\omega}^b \times (\mathbf{x}_i^a - \mathbf{x}_c^b), \tag{9}$$

where v^a , v^b , ω^a , and ω^b are the linear and angular velocities of particle a and particle b, respectively. The increment in shear displacement Δs_i has the following form:

$$\Delta s_i = \left[\mathbf{v}^{a,b} - \left(\mathbf{v}^{a,b}.\mathbf{n}_i^{a,b} \right) \mathbf{n}_i^{a,b} \right] \Delta t, \tag{10}$$

where Δt is the time interval. The tangential contact force $F_{s,i}^a$ exerted on particle a at contact node i is calculated by:

$$\left(\boldsymbol{F}_{s,i}^{a}\right)_{t+\Delta t} = Z\left(\boldsymbol{F}_{s,i}^{a}\right)_{t} - k_{s}\Delta s_{i},\tag{11}$$

where k_s is the shear elastic stiffness. Coulomb friction law limits tangential contact force $F_{s,i}^a$ to be no greater than a fraction of the normal contact force $F_{n,i}^a$:

$$F_{s,i}^{a} = \frac{F_{s,i}^{a}}{\|F^{a}_{s,i}\|} \min(\|F_{s,i}^{a}\|, \mu\|F_{n,i}^{a}\|), \tag{12}$$

where μ is the interparticle friction coefficient. Similarly, the tangential contact force $F_{s,i}^b$ exerted on particle b at contact node i is calculated as:

$$F_{s,i}^b = -F_{s,i}^a. (13)$$

The resulting moments $M^a_{s,i}$ and $M^b_{s,i}$ at contact node i are calculated as:

$$\mathbf{M}_{si}^{a} = (\mathbf{x}_{i}^{a} - \mathbf{x}_{c}^{a}) \times \mathbf{F}_{si}^{a}, \tag{14a}$$

$$\mathbf{M}_{si}^b = (\mathbf{x}_i^a - \mathbf{x}_s^b) \times \mathbf{F}_{si}^b. \tag{14b}$$

Eventually, the total contact forces and moments generated by the contact of particle a and particle b are expressed as:

$$\mathbf{F}^{a} = \sum_{i=1}^{N} \left(\mathbf{F}_{n,i}^{a} + \mathbf{F}_{s,i}^{a} \right), \tag{15a}$$

$$M^{a} = \sum_{i=1}^{N} \left(M_{n,i}^{a} + M_{s,i}^{a} \right),$$
 (15b)

$$\mathbf{F}^{b} = \sum_{i=1}^{N} \left(\mathbf{F}_{n,i}^{b} + \mathbf{F}_{s,i}^{b} \right), \tag{15c}$$

$$\mathbf{M}^{b} = \sum_{i=1}^{N} \left(\mathbf{M}_{n,i}^{b} + \mathbf{M}_{s,i}^{b} \right), \tag{15d}$$

where N is the total number of the contact nodes between particle a and particle b. When particle b is replaced by a wall, we can calculate the particle—wall interaction $F_{w,p}$ generated by the contact of particle a and a wall. In DEM, the motion of one particle is controlled by Newton's second law. All the relevant calculations for the motion of particles can be found in the classical literature of mechanics (Cundall and Strack, 1979; Evans and Murad, 2006; Goldstein, 2001; Hart et al., 1988; Walton and Braun, 1993).

2.3. Coupled CFD-iDEM

There are many cases in which particle movement happens with the presence of fluid phase or even is induced by fluid phases, such as fluidization, Pneumatic conveying, and natural hazards. Under these circumstances, the fluid-particle interaction plays an enormous role in determining the dynamics of granular particles submerged in a fluid. Such phenomena are simulated by coupling the DEM and CFD methods (Tsuji et al., 2008; Zhang and Tahmasebi, 2019, 2018; Zhao et al., 2016). In this coupling scheme, the fluid flow is simulated by Navier-Stokes equations with an extra force term of the fluid-particle interaction, and the particle movement is simulated by the typical DEM with an extra force term of the fluid-particle interaction. Therefore, the coupled dynamics of the fluid and solid phase is achieved by considering the extra force term of the fluid-particle interaction. With the ability of our proposed iDEM method to capture the complex morphologies, we propose using CFD-iDEM to simulate the movement of natural particles with the presence of fluid. With the merit of considering the irregular particle shape, CFD-iDEM improves the range of applications and makes simulation results more accurate and physically realistic. To achieve this goal, we consider the total computational domain Ω , including particle domain Ω_p and fluid domain Ω_f . The fluid boundary not shared with the particle domain is denoted by Γ_f , and the fluid-particle interface, that is the particle boundary, is denoted by Γ_p . Considering incompressible Newtonian fluid, the governing equations for the fluid motion are given

$$\nabla . \boldsymbol{u} = 0 \mathrm{in} \Omega_f \tag{16a}$$

$$\rho\left(\frac{\partial \mathbf{u}}{\partial t} + (\mathbf{u}.\nabla)\mathbf{u}\right) = \nabla.\mathbf{\sigma} + \rho g \nabla \sin\Omega_f$$
(16b)

where u, and ρ are the velocity and the density of the fluid, respectively. g is the gravitational acceleration. σ is the stress tensor, which has the following form:

$$\sigma = -pI + \tau, \tag{17}$$

where p is the pressure. I is the identity tensor, and τ is the viscous stress tensor. For an incompressible Newtonian fluid, $\Delta \sigma$ is given by:

$$\nabla . \sigma = -\nabla p + \mu \Delta u, \tag{18}$$

where μ is the viscosity of the fluid. The boundary and initial conditions are described by:

$$\mathbf{u} = \mathbf{u}_{\partial\Omega_f}(t)$$
 on Γ_f (19a)

$$\mathbf{u} = \mathbf{u}_i \quad \text{on} \Gamma_p \tag{19b}$$

$$\boldsymbol{\sigma}.\boldsymbol{n} = \boldsymbol{t}_{\partial\Omega_p} \quad \text{on}\Gamma_p \tag{19c}$$

$$\boldsymbol{u}(t) = \boldsymbol{u}_0 \quad \text{in}\Omega_f \tag{19d}$$

where u_i is the velocity of the fluid-particle interface. n is the outer normal direction on the particle surface. $t_{\partial\Omega_p}$ is the traction vector exerted on the particle surface by the fluid.

The governing equation for particles with the presence of fluid is similar to Eq. (3), with the only difference being an extra term, that is fluid-particle interaction, added:

$$m_p \frac{du_p}{dt} = m_p g + \sum_{N_p} F_{p,p} + \sum_{N_w} F_{w,p} + F_{f,p},$$
 (20)

where $F_{f,p}$ is the total fluid-particle interaction exerted on the particle. First, we consider the calculation in the CFD part, which is based on the idea of Fully Resolved Simulation (FRS). The details of the FRS are well documented elsewhere (Patankar et al., 2000; Shirgaonkar et al., 2009). The calculation in the CFD part includes three steps:

The total computational domain Ω is regarded as the fluid phase and an intermediate velocity field \hat{u} is computed by solving the incompressible Navier-Stokes equations, which has the following form:

$$\rho\left(\frac{\partial \widehat{\boldsymbol{u}}}{\partial t} + (\widehat{\boldsymbol{u}} \cdot \nabla)\widehat{\boldsymbol{u}}\right) = -\nabla p + \mu \Delta \widehat{\boldsymbol{u}} + \rho g \nabla z. \tag{21}$$

2. In the particle area, the intermediate velocity field \hat{u} is corrected by imposing the particle's velocities provided by the DEM simulation. The correction leads to a new velocity field u, which is equivalent to adding a new force term f:

$$f = \rho \frac{u - \hat{u}}{\Delta t}.$$
 (22)

Then, \hat{u} is corrected to u(=particle velocity $u_p)$ and f is non-zero only in the solid domain. Here, u_p is composed of the translational and rotational components:

$$\boldsymbol{u}_p = \boldsymbol{v}_p + \boldsymbol{r} \times \boldsymbol{\omega}_p, \tag{23}$$

where v_p is the translational velocity of the particle; r is the distance vector pointing from the mass center of the particle to the center of the fluid cell, which is occupied by the particle, and ω_p is the angular velocity.

3. It should be noticed that step 2 introduces a discontinuity in velocity at the fluid-particle interface, which results in a non-zero divergence at the fluid-particle interface. Hence, final velocity field u, which is divergence-free, is obtained by a scalar field ϕ :

$$u = u - \nabla \phi, \tag{24}$$

where ϕ is calculated by the following Poisson equation:

$$\Delta \phi = \nabla . u. \tag{25}$$

Similarly, the manipulation of the velocity field (only in the solid domain) is equivalent to adding an extra pressure term:

$$\rho \frac{\mathbf{u} - \mathbf{u}}{\Delta t} = -\rho \frac{\nabla \phi}{\Delta t},\tag{26}$$

The substitution of Eq. (22) and Eq. (26) into Eq. (21) leads to:

$$\rho\left(\frac{\partial \mathbf{u}}{\partial t} + (\mathbf{u}.\nabla)\mathbf{u}\right) = -\nabla p^* + \mu \Delta \mathbf{u} + \mathbf{f} + \rho g \nabla z, \tag{27}$$

where the corrected pressure p^* is $p + \frac{\rho\phi}{\Delta t}$.

Then, we consider the iDEM simulation for particle motion. The key

to calculating the force exerted on particles by a fluid is to include the fluid-particle interactions $F_{f,p}$ into the iDEM simulation. The fluid-particle interaction exists at the fluid-particle interface, which can be calculated by the integration of fluid force over the particle's surface Γ_p (Hager et al., 2014):

$$\mathbf{F}_{f,p} = \int_{\Gamma_p} \mathbf{t}_{\partial\Omega_p} d\Gamma_p = \int_{\Gamma_p} (-p\mathbf{I} + \boldsymbol{\tau}) \cdot \mathbf{n} d\Gamma_p, \tag{28}$$

 \boldsymbol{n} is the outer normal direction on the particle surface. Combining the divergence theorem leads to:

$$\int_{\Gamma_p} (-p\mathbf{I} + \boldsymbol{\tau}) \cdot \mathbf{n} d\Gamma_p = \int_{\Omega_p} \nabla \cdot (-p\mathbf{I} + \boldsymbol{\tau}) d\Omega_p.$$
 (29)

The integration can be rewritten as:

$$F_{f,p} = \int_{\Omega_p} (-\nabla p + \mu \Delta u) d\Omega_p. \tag{30}$$

Here, we apply the CFD method to obtain the numerical solutions for the fluid phase, which means the fluid phase is analyzed in discrete fluid meshes. Eq. (30) can be, therefore, transformed into a discretization form with the extension from the integration over the particle domain to the integration over the whole fluid–solid domain Ω :

$$\int_{\Omega_p} (-\nabla p + \mu \Delta \mathbf{u}) d\Omega_p = \int_{\Omega} (-\nabla p + \mu \Delta \mathbf{u}) \delta_{\Omega_p} d\Omega.$$
 (31)

Considering an arbitrary element x in the domain Ω , δ_{Ω_n} is defined as:

$$\delta_{\Omega_p} = \begin{cases} 1if \mathbf{x} \in \Omega_p \\ 0else \end{cases} \tag{32}$$

Numerical integration in the whole domain leads to:

$$\mathbf{F}_{f,p} = \sum_{i=1}^{N} \left(-\nabla p + \mu \Delta \mathbf{u} \right)_{i} V_{i}, \tag{33}$$

where N is the total number of the fluid cells which is covered by the particle. V_i is the volume of cell i. The other steps in the iDEM, such as the calculation of particle–particle interaction $F_{p,p}$, the update of particle motion, will remain unchanged.

The key to accomplishing the coupled CFD-iDEM is to successfully identify the particle in the computational fluid cells. Considering the complex morphology of the particles in our study, we have proposed a numerical algorithm to evaluate the particle volume in fluid cells, which is currently applied for hexahedral cells:

Step 1: Divide one particle into small cubes, shown in Fig. 5(b),

Step 2: Assign the particle volume to each of these small cubes. The particle volume in one cube is determined by the vertex number of one cube. One vertex, which exists inside the particle, contributes to the stored volume by one-eighth of the cube volume. Therefore, if all the eight vertices of one cube exist inside the particle, the particle volume stored in the cube equals the cube volume. The decision of the position status of one vertex ve_i ($i = 1, 2 \cdots 8$) inside or outside of the particle is determined by $\Phi(ve_i)$: a negative value means inside of the particle while positive means outside of the particle, where Φ represents the distance map of the particle.

Step 3: Assign the particle volume to the fluid cells, which requires identifying the particle in the fluid cells as follows:

Find the fluid cell that contains the center position of the particle.
 When it comes to the parallel simulation, the center position will be supplemented by the particle surface nodes because the center position only exists in one processor. The fluid cell (one corresponding to each processor in the parallel simulation) is called the first particle-occupied cell.

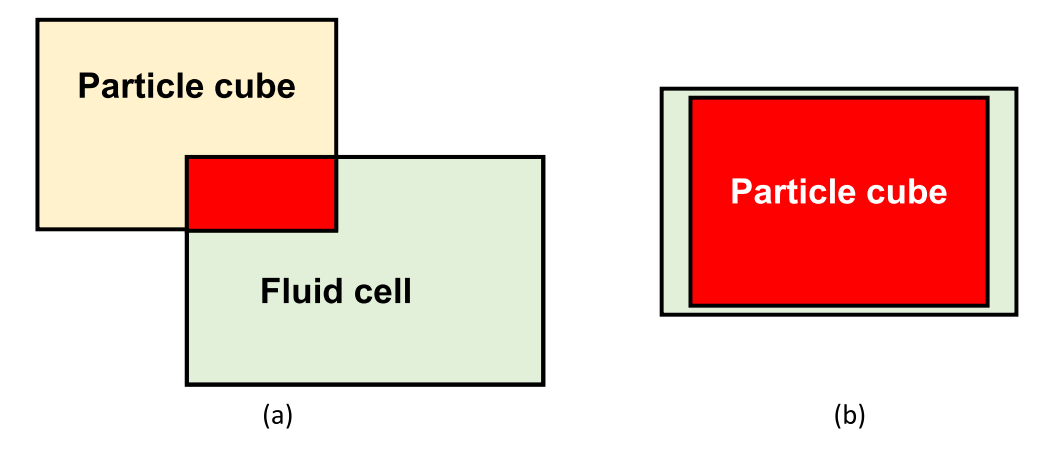


Fig. 4. The illustration of the overlap between the particle cube and fluid cell. partially overlapped (a) and fully overlapped (b).

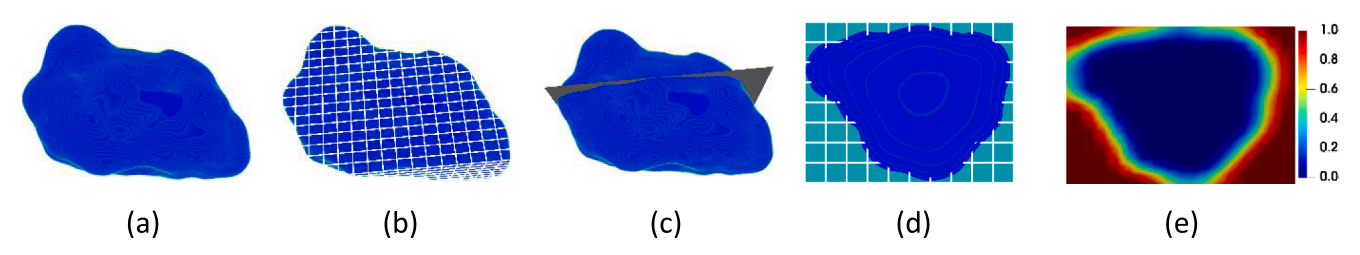


Fig. 5. Illustration for the identification of one particle in the computational fluid cells. (a) One irregular particle and (b) division of the particle into small cubes. (c) 2D slice from the particle and (d) the location of the slice in fluid cells. (e) Calculated void-fraction based on the slice.

- Based on the first particle-occupied cell, the loop to detect more fluid cells occupied by the particle starts by examining if the six neighbor cells of the first particle-occupied cell contain a part of the particle.
- If one neighbor cell is determined to contain a part of the particle, the six neighbor cells of the neighbor cell will be examined as well.
 Otherwise, there will be no further examination on the neighbor cells of this neighbor cell. The fluid cells containing the particle are all detected when no neighbor cell in the whole computation domain needs to be examined.
- The particle volume contained in the fluid cells is the key to continuing or terminating the loop: if the particle volume contained in one fluid cell is bigger than zero, a part of the particle is detected in this fluid cell and the loop continues with the neighbor cells. The overlap volume between the particle cube and fluid cell (as shown by the red part in Fig. 4) represents how much of the particle volume stored in the particle cube can be assigned to the fluid cell. For example, if the particle cube is fully involved in the fluid cell, the fluid cell will obtain the whole particle volume stored in the particle cube, as shown in Fig. 4(b). At the end of the cell search loop, the fluid cells containing the particle are all detected, and the particle volume is assigned to these fluid cells, as shown in Fig. 5(e) (the fraction of particle volume = 1 void-fraction).

3. Model simulations

Based on the X-ray computed tomographic (XRCT) image data, we used an improved distance transformation to depict particles by distance values (see Section 2.1). In other words, the virtual specimen, whose particles are the same as the actual particles in both shape, position, and properties, is generated by the enhanced distance transform characterization and is used in the motion simulation (see Section 2.2). With all the particle data prepared, the image-based DEM (iDEM) is used to simulate the motion of real irregular particles. Finally, a coupled system in which the domain is composed of solid particles and fluid is simulated to capture the dynamic behavior of both the fluid and particles (see

Section 2.3). With the XRCT image data of a sandstone sample, we apply the enhanced distance transform (EDT) to convert them to distance fields and generated 20 granular assemblies containing 288 particles with different irregularities. It should be noted that such particles, if XRCT data are not available, can be produced using stochastic modeling as well (Tahmasebi, 2018a, 2018b). Fig. 6 shows the distribution of particle sphericity (S) and roundness (R) for all the produced granular assemblies (Krumbein, 1941; Powers, 1953; Wadell, 1932). Krumbein defined the sphericity as:

$$S = \sqrt[3]{bc/a^2},\tag{34}$$

where a for the long axis, b for the intermediate axis, and c for the short axis of the three representative axes of one particle. Wadell defined the roundness as the ratio of the average radius of curvature of the corners of one particle to the radius of its maximum inscribed sphere:

$$R = \frac{\frac{1}{n} \sum_{i=1}^{n} r_i}{r_{max-in}},\tag{35}$$

where r_i is the radius of the i-th corner curvature, n the number of corners, and r_{max-in} the radius of the maximum inscribed sphere. It can be observed that the shape of particles gradually changes from irregular to regular spheres from both Fig. 6 and Fig. 2 (in Section 2.1). It should be noticed that the individual particle mass (with the unit of kg) in different assemblies is the same, with a relative error of less than 5×10^{-5} , calculated by:

$$masserror = \left| \frac{m_{s,i} - m_{s,1}}{m_{s,1}} \right|, i = 2, 3, \dots, 20$$
(36)

where $m_{s,i}$ is the mass of one particle in the first particle assembly, and $m_{s,i}$ is the mass of the corresponding particle in the i-th particle assembly). Here, we set the friction coefficient for the first granular assembly, as the most irregular, to be 0.5, and the friction coefficient for the last granular assembly, which is the spherical particles, as 0.25. The friction

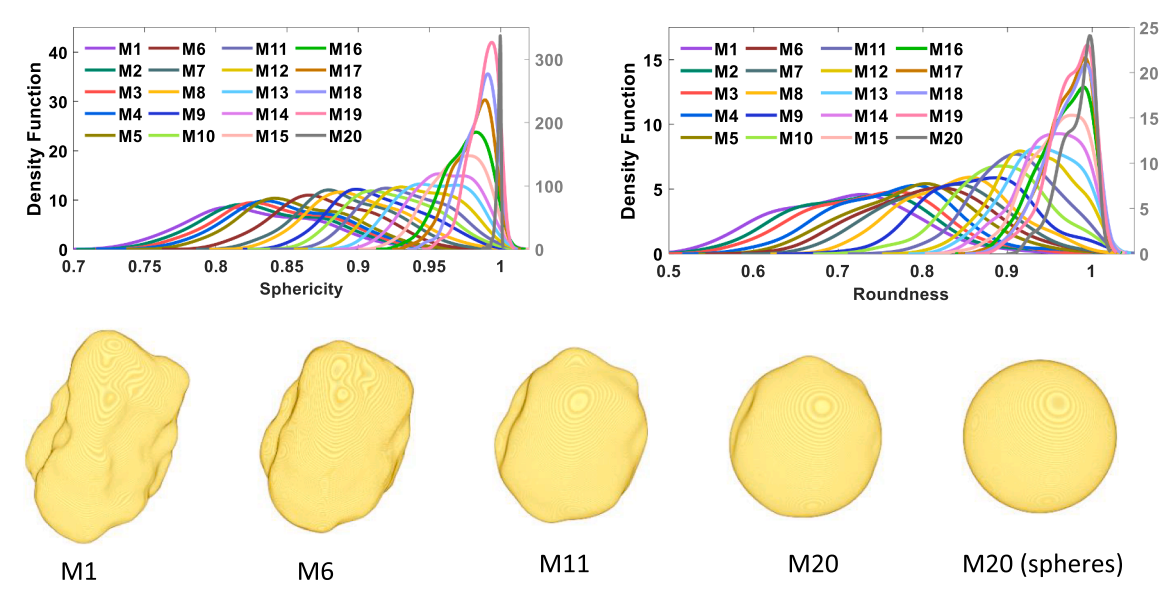


Fig. 6. The sphericity and roundness of different morphologies (upper row). Morphological representation of a random particle with five distinct shapes (lower row).

coefficients for the rest of the assemblies are determined by linear interpolation between particle roundness and friction angle (Cho et al., 2006; Minsu et al., 2014).

Using our computational method, we performed the collapse simulation for all granular assemblies containing 288 particles with no fluid. Furthermore, the collapse behavior of all granular assemblies with the presence of a fluid (here, water) is also simulated and studied. For the dry cases, the simulations are operated based on our proposed iDEM while a coupled scheme, namely CFD-iDEM, is used for the wet cases to consider the effect of fluid. The key to achieving the CFD-iDEM coupling is to transfer the particle information, such as mass, shape, position, and velocity, etc., into the fluid domain and exert the fluid force on particles. The motion state of particles affects the fluid flow behavior, which in turn exerts forces on the particles. The detailed theories are referred to the Section 2.3. The spatial distribution of the considered particles for each assembly follows a certain pattern: six particles along the x-direction (horizontal direction), one particle along the y-direction and there are two vertical walls to constrain the y-directional particle motion, and 48 particles along the z-direction (vertical direction). The average diameters of individual particles in all assemblies range from 0.8 mm to 0.9 mm with the same density of $\rho_s=2.5\times 10^3~{\rm kg/m^3}.$ It should be noted that the average particle diameter is calculated based on the particle mass, that is $d_s = 2 \times \left(\frac{3m_s}{4\pi\rho}\right)^{1/3}$, where d_s is the average diameter

(with the unit of m) and m_s is the mass of one particle (with the unit of kg). Furthermore, we considered water as the fluid in this study with the density $\rho_f=1\times 10^3~{\rm kg/m^3}$ and the kinematic viscosity $v_f=1\times 10^{-6}~{\rm m^2/s}$. The fluid flow is solved numerically, where an Euler scheme for $\partial/\partial t$, Gauss linear for gradient and divergence, and Gauss linear corrected for Laplacian ∇^2 are used. While the DEM solver updates the particle motion, the PISO (Pressure-Implicit with Splitting of Operators) algorithm is applied for solving the Navier-Stokes equations in the CFD-solver. A no-slip boundary condition is used in all the wet simulations.

Before discussing the results for a complex case with angular particles, let us verify the accuracy of our proposed method for spherical particles as one can find several such studies using analytical and numerical solutions. Thus, we have tested the simulation of one particle settlement with different contact parameters (normal stiffness k_n) and global damping parameters, as shown in Figs. 7 and 8. It can be observed that the simulation results of one particle settlement have a great agreement with the results of Glowinski et al. with the global damping

being 15 (Glowinski et al., 2001; Hager, 2014). Considering that the contact interaction is generated only when the particle hits the bottom wall, Fig. 8 plots the comparison of velocity (time from 0.35 s to 0.5 s) of different normal stiffness $k_n = 2, 1, 0.5$ (kN/m) with the global damping being 15. Moreover, the shear stiffness k_s is determined based on the normal stiffness k_n : $k_s = \frac{k_n}{2(1+\nu)}$, where ν is Poisson's ratio and is set as 0.25 in our paper. It can be observed that there is a negligible difference in the particle velocity, which can be explained by the number of contact nodes. This also can be automatically adjusted with different normal stiffness: more contact nodes with smaller normal stiffness; fewer contact nodes with larger normal stiffness. Therefore, the contact interaction of particle-particle or particle-wall calculated in this study is rather robust. Considering that the global damping plays an important role in dissipating the energy of the granular system, we have chosen the global damping being 20 in the main example described in this paper, namely collapsing of a column of particles, which is more complicated than the one particle settlement problem.

Fig. 9 displays successive velocity snapshots of the collapse of dry models (three time-steps $t=0\ s,\ 0.075\ s,\ and\ 0.175\ s)$ and wet models (three time-steps $t=0.0125\ s,\ 0.15\ s,\ and\ 0.3\ s)$ for the M1 and M20 (spheres) assemblies. It shows that the grains collapse vertically (z-direction) first, spread horizontally (x-direction), and finally, stop after traveling a certain distance. It is also observed that the runout distance, that is the spread distance of particles on the x-direction, elevates as the regularity of particles increases for both dry and wet models (Topin et al., 2012). The difference in the runout distance of the assemblies in the dry state is much more distinct than that of the wet state. Next, we will discuss the collapse further based on more analyses.

With the numerical simulations, we have obtained the movement information at various time intervals, such as positions, displacements, and velocities of particles. Note that the results are dimensionless: using d for length normalization, $\sqrt{d/g}$ for time normalization, mg for force normalization, and mgd for energy normalization. Here, d is the average diameter of one assembly, m is the average mass of one assembly, and g is the gravitational acceleration. Fig. 10 shows the grain trajectories together with the vertical and horizontal mean kinetic energy calculated by:

$$E_z = \frac{mv_z^2}{2}, \text{and} E_x = \frac{mv_x^2}{2}.$$
 (37)

Here, the mean kinetic energy refers to the arithmetic mean estimator

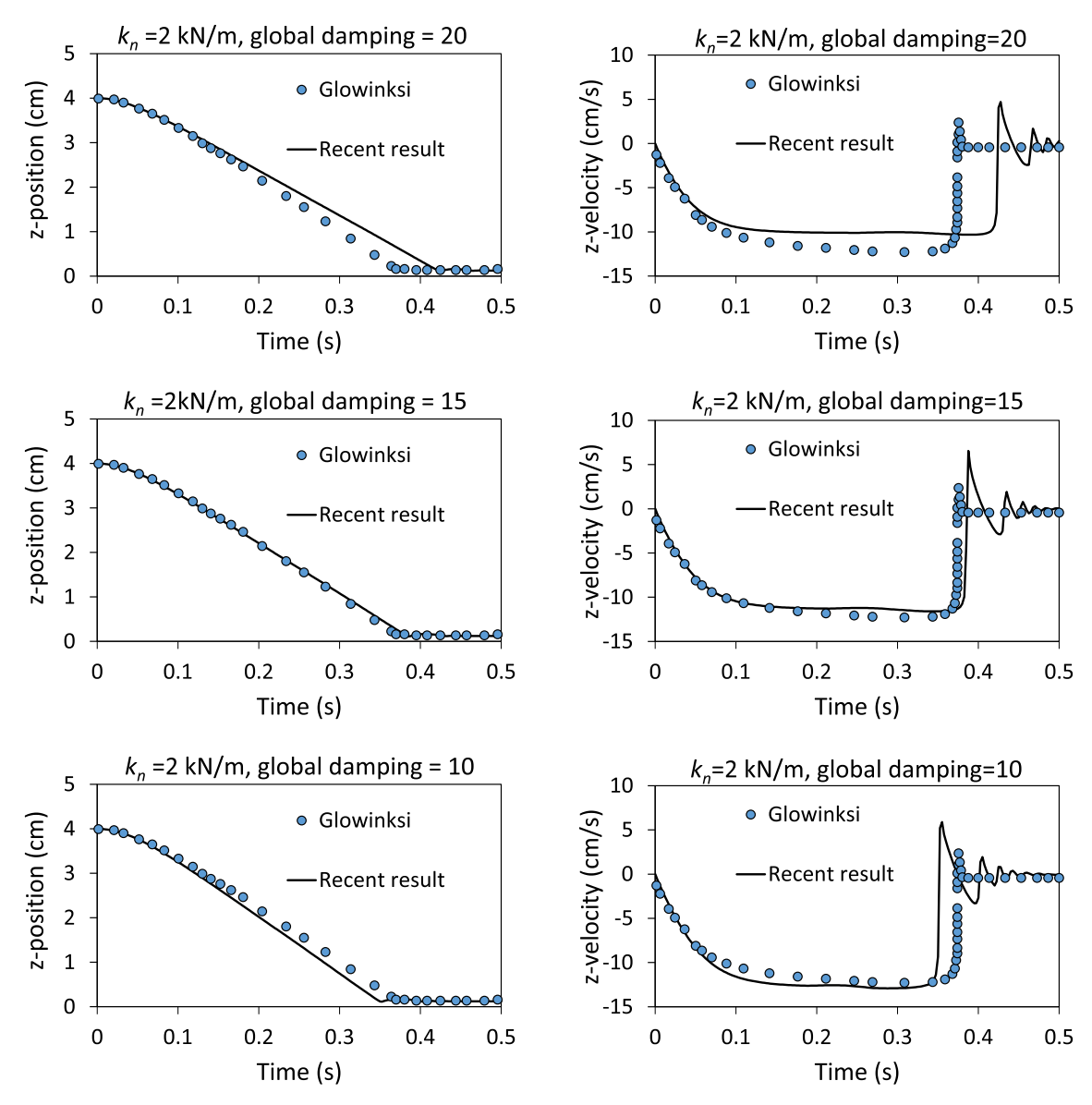


Fig. 7. The particle position (left) and velocity (right) in the vertical direction of a settling particle of density $1.5 \times 10^3~kg/m^3$ and diameter 0.25 cm in a fluid with viscosity $1 \times 10^{-6}~m^2/s$.

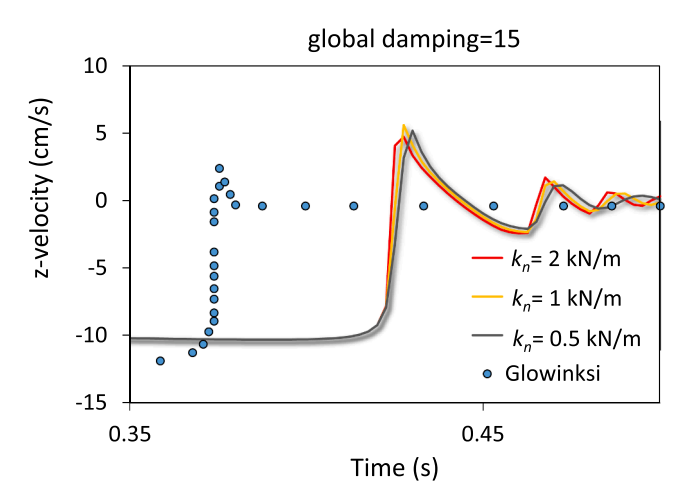


Fig. 8. The comparison of the particle vertical velocity after the particle hits the bottom wall with different normal stiffness.

over a single assembly. In the dry models, the grain trajectories and the evolution of mean kinetic energy (E_z and E_x) show that the horizontal movement of M20 assembly (i.e., spheres) is much larger than that of M1 (most irregular shape) while there is a negligible difference in the vertical direction. Although there is also an obvious horizontal difference between M1 and M20 assemblies in the wet cases, such a difference is greatly mitigated by the presence of the fluid, which does not allow the particles to travel a longer distance. Compared with the dry cases, the fluid in the wet cases more effectively blocks the horizontal movement of M20 than that of M1. The presence of fluid prolongs the life of E_z and E_x , which is the reason why the vertical displacement of the dry and wet cases is similar when the maximum of E_z in the wet cases is much smaller than that of the dry cases.

Once the simulations are complete (i.e., t=0.45 s), the grain final displacements, as shown in Fig. 11(a) and 8(b), are obtained for the dry and wet assemblies (M1-M20). In the dry cases, the *x*-direction (horizontal) displacements gradually increase as the regularity of particles enhances. There is also a small increase in the *z*-direction (vertical) displacements when the particles become more regular. In the wet cases, both the horizontal and vertical displacements are impeded: the

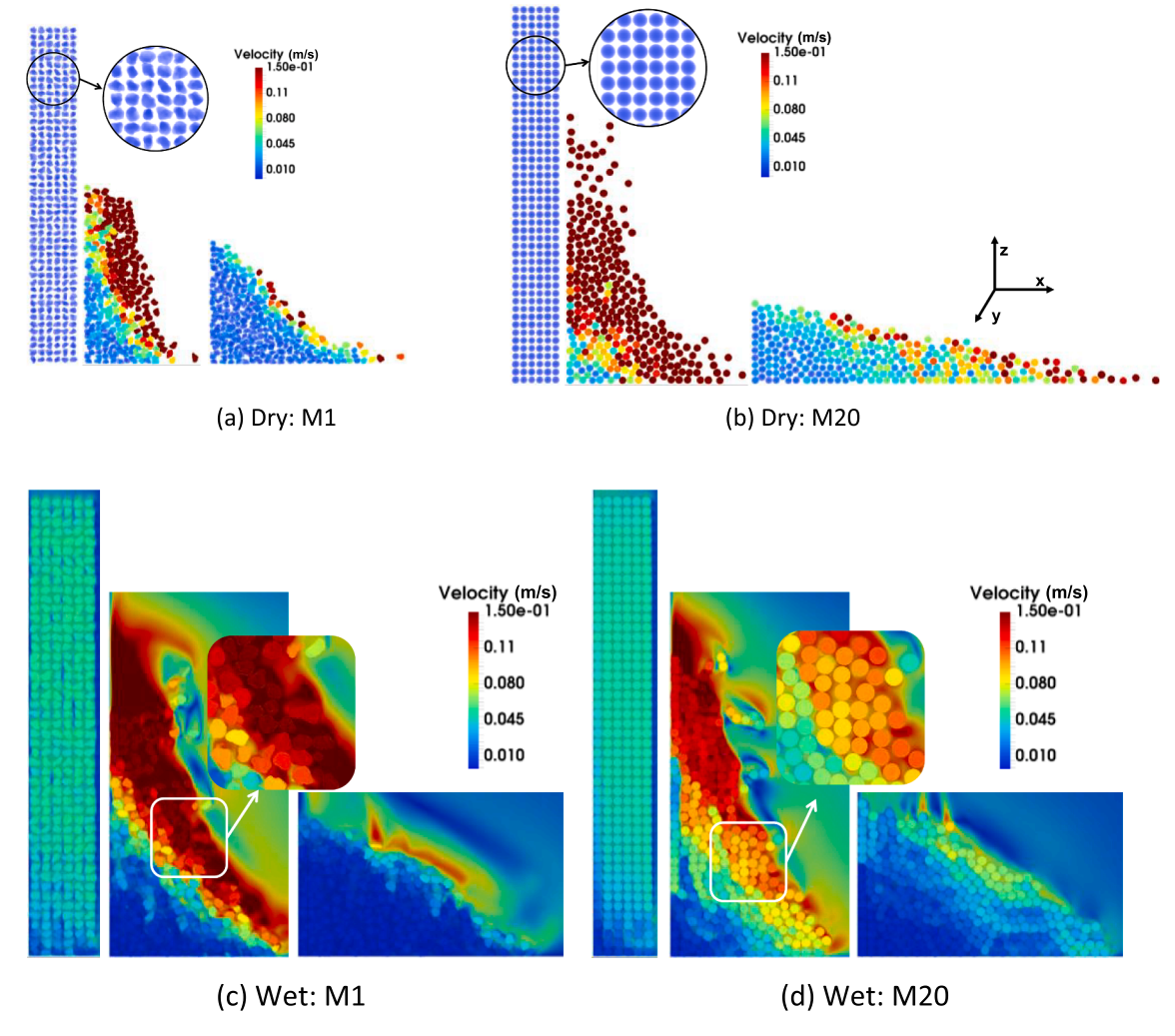


Fig. 9. Successive velocity snapshots of the collapse for M1 and M20 (spheres) assemblies of dry and wet cases.

horizontal displacements slowly increase with rising the regularity of particles while the vertical displacements are similar. Moreover, the displacement comparison between dry and wet cases shows that both the horizontal and vertical displacements of the dry models become larger than the corresponding wet models with enhancing the regularity of particles, which reflects that there are more viscous effects on the high regular particles and therefore greatly impedes the movement of such particles. For the first six assembles (M1, M2, ..., M6), it is interesting to observe that the horizontal displacement of the wet models is larger than that of the dry samples. The movement difference between the dry and wet models indicates that the particle movement with a fluid is both impeded and enhanced by the viscous and lubrication effects. The larger horizontal displacement in the wet cases (M1, M2, ..., M6) indicates that the lubrication effect exerted on the highly irregular particles by the fluid surpasses the viscous effect.

It can be observed that the horizontal and vertical displacements of both the dry and wet models are greatly affected by the regularity of particles. Moreover, we have found that particle sphericity is more relevant to particle movement. Fig. 11(c) and 8(d) exhibit a good correlation between particle movement and sphericity. The coefficients α in the exponential fitting function (can be expressed by $x_{disp} = \beta e^{\alpha S}$) quantifies the dependence level of particle movement in the horizontal direction on the sphericity. The coefficient of α (7.0649) in the dry cases is larger than the α (2.6209) in the wet cases, which reflects that the presence of fluid alleviates the movement discrepancy caused by particle morphology. The coefficient β in the fitting function predicts the particle

movement in the horizontal direction under extreme morphological conditions (sphericity = 0). The coefficient of β (0.0117) in the dry cases is smaller than the β (0.5968) in the wet models, which indicates that the highly irregular particles in the wet cases are more active than the dry circumstance because of the fluid lubrication effect.

Fig. 12(I) shows the mean kinetic energy for both the dry and wet cases (e.g., M1, M6, M11, M15, M20). It can be observed that the horizontal component of mean kinetic energy (E_x) increases as the particles become more regular in the dry cases. The vertical component of mean kinetic energy (E_z) in the dry cases, however, is similar for different particle morphologies. In the wet cases, the difference of the horizontal mean kinetic energy caused by the particle shape is not obvious, but the vertical mean kinetic energy tends to decrease by enhancing the regularity of particles, which reflects the larger obstruction effect of fluid on the more regular particles. Moreover, the values of the mean kinetic energy in the wet cases are smaller than that of the dry cases, which is due to the fluid viscous effect. Furthermore, it can be seen that the E_x becomes zero around $t/(d/g)^{0.5}=25$ in the dry cases while the curves meet zero at around $t/(d/g)^{0.5} = 50$ in the wet cases, which implies that the lifespan of particle movement is sustained by the fluid lubrication effect, and particles can keep the energy for a longer time instead of a rapid release. This finding can be important for natural hazards as the wet environment may cause more serious and longer threats. Fig. 12(II) displays the maximum of horizontal and vertical components of mean kinetic energy in both the dry and wet models. It can be observed that only the maximum of horizontal mean kinetic energy in the dry cases

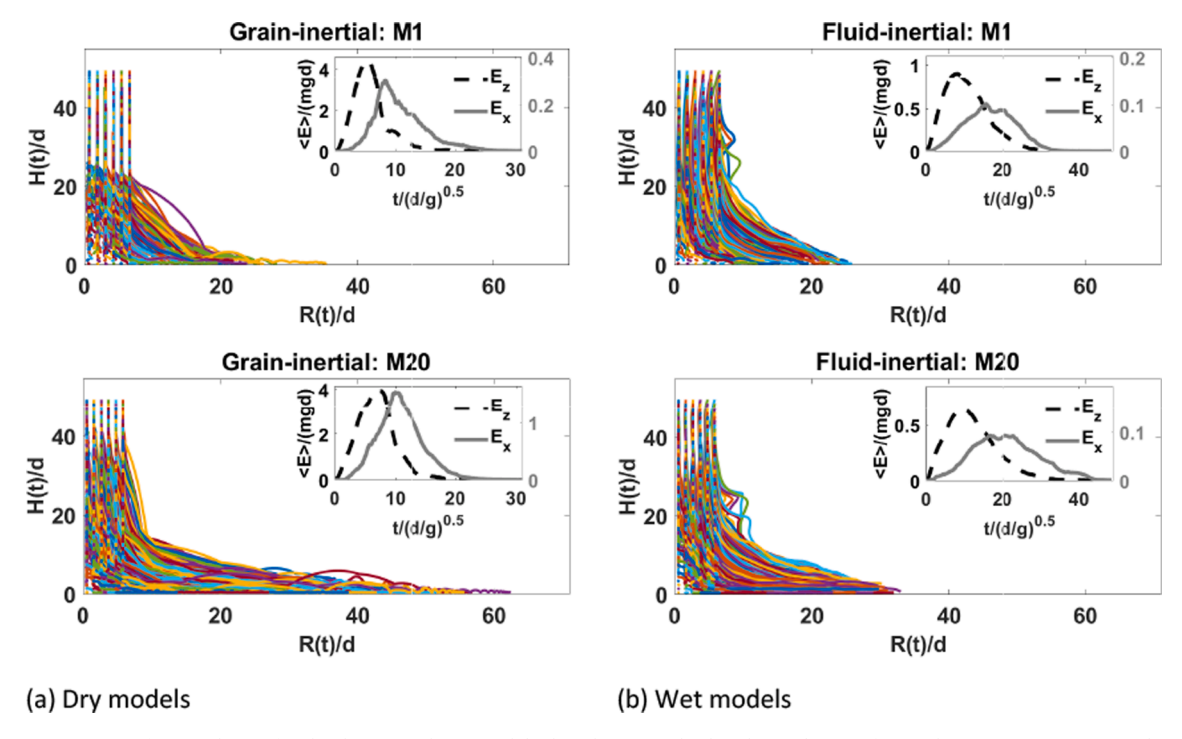


Fig. 10. Grain trajectories of M1 and M20 for the dry (a) and wet models (b). The insets display the evolution of mean kinetic energy per particle carried by the vertical (z) and horizontal (x) components.

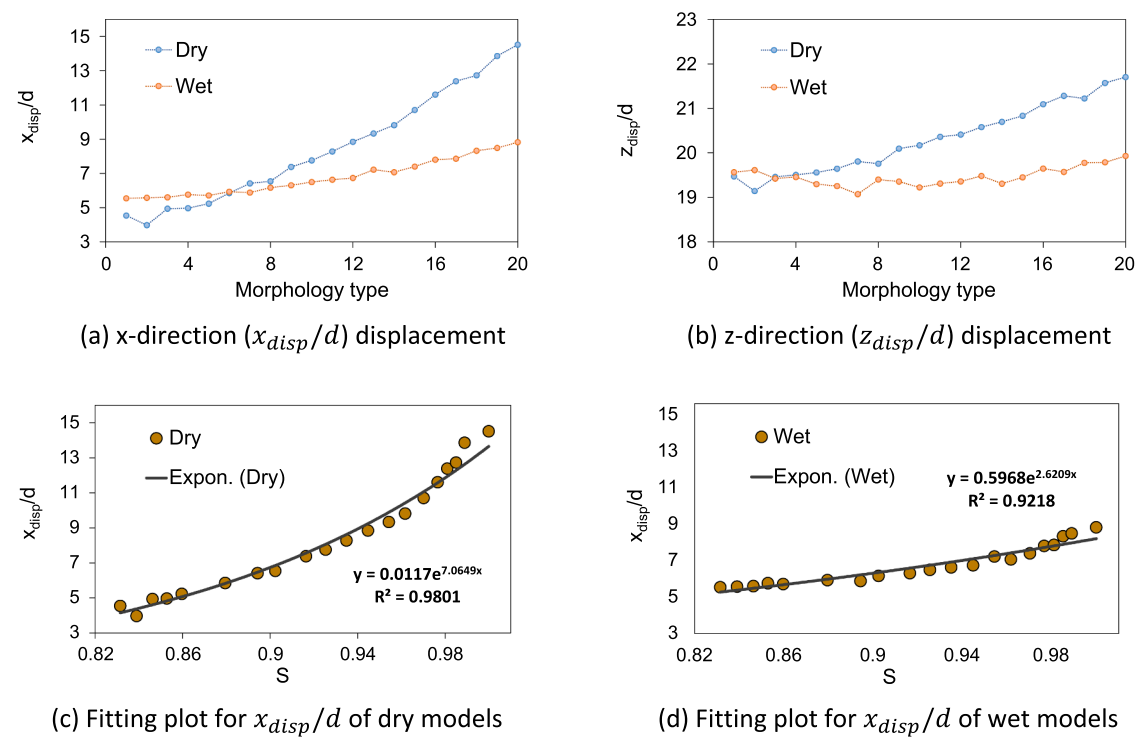


Fig. 11. Plots of grain displacement for both dry and wet models.

increases as the regularity of particles enhances. By increasing the regularity of particles, the discrepancy of horizontal mean kinetic energy triggered by distinct morphologies is diminished as the fluid effect increases, which results in dipping the vertical mean kinetic energy. The change of kinetic energy from dry to wet cases, again, is highlighting the phenomenon that the presence of fluid can lighten the movement

difference induced by different particle shapes.

4. Conclusion

The morphology of particles has a great effect on the dynamic behavior of granular particles. Our collapse results show that the

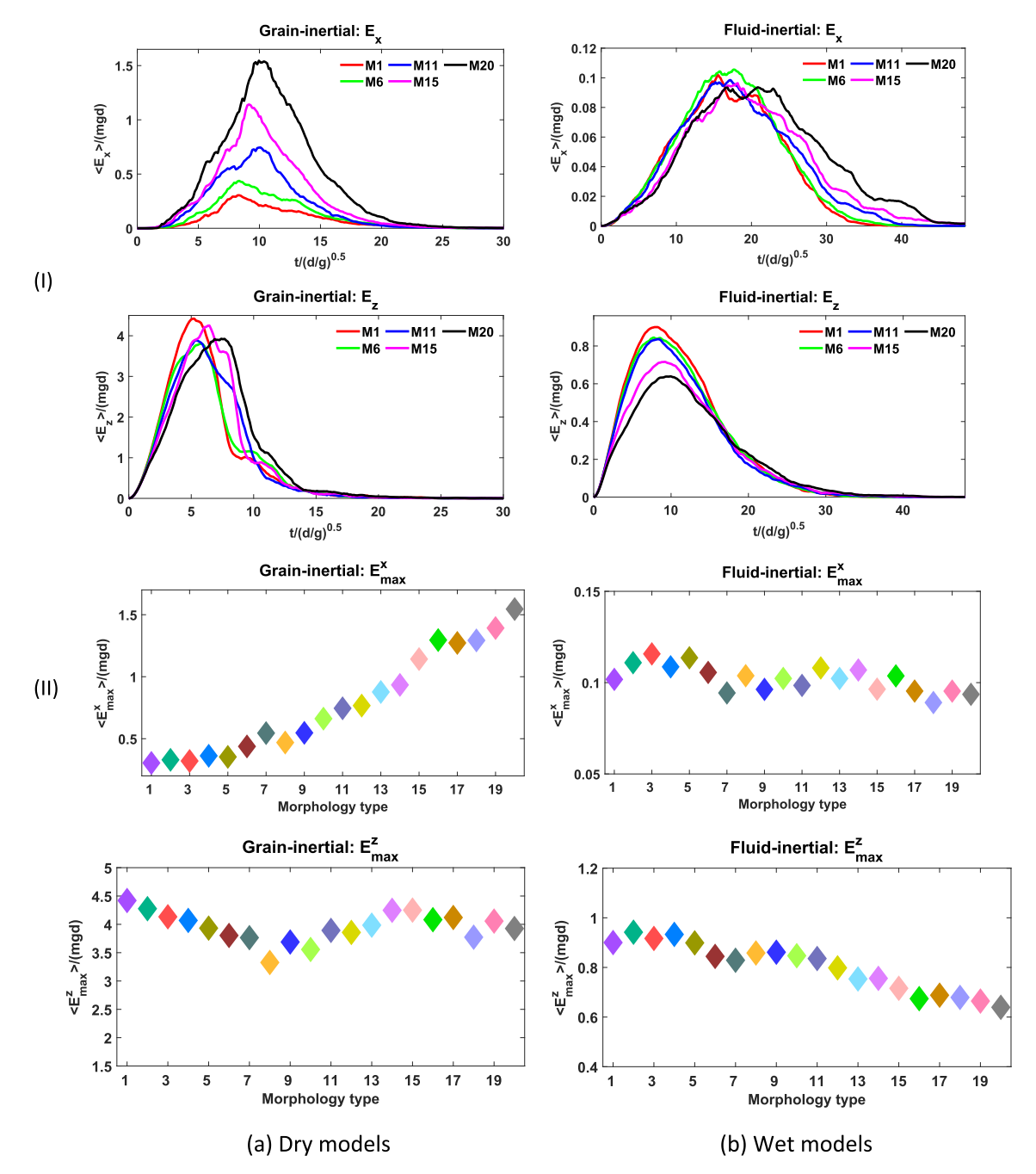


Fig. 12. (I) Horizontal and vertical mean kinetic energy: E_x/mgd , E_z/mgd and (II) maximum of horizontal and vertical mean kinetic energy: E_{max}^x/mgd , E_{max}^z/mgd for dry (a) and wet (b) cases.

horizontal displacement increases with the growing regularity of particles in dry models while the presence of fluid mitigates the difference. The vertical displacement slightly increases with enhancing the regularity in the dry cases while the effect of particle shape on the vertical movement is negligible compared with the fluid effect in the wet cases. The fluid can both impede and enhance the movement of particles by the viscous and lubrication effects, respectively. Compared to fluid lubrication, the fluid viscous effect becomes dominant when the morphology of particles becomes more regular.

It is found that the displacements of particles in both dry and wet cases have a good correlation with the sphericity: exponential relation on the horizontal direction. The coefficient α in the exponential linear fitting function, which reflects the dependence level of particle movement in the horizontal direction on the sphericity, is larger in the dry

cases compared to the wet cases. The smaller coefficient α reveals the fact that the presence of fluid alleviates the movement difference caused by the morphology of particles. The coefficient β in the exponential fitting function is larger in the wet cases than the dry models, which indicates that the fluid lubrication effect becomes dominant with highly irregular particles. Therefore, such particles in wet systems are more active and experience more movement than the dry circumstance (e.g., M1, M2, ..., M6).

The horizontal component of E_x increases as particle regularity enhances in the dry cases while no obvious difference in the vertical component of E_z is observed. In the wet cases, the values of the mean kinetic energy are smaller due to the impediment exerted on particles by the fluid viscous effect while the lifespan of the mean kinetic energy is much prolonged owing to the fluid lubrication effect. By increasing the

regularity of particles, the discrepancy of horizontal mean kinetic energy triggered by distinct morphologies is diminished as the fluid effect increases, which results in dipping the vertical mean kinetic energy. The results of this study shed a light on complex problems related to irregular particles immersed in the fluid and allow one to predict the collapse-related movement, such as landslides, avalanches, and debris flows, and help to reduce natural damage and economic losses. Furthermore, as mentioned, the results are quite generic and can be used in other fields related to granular particles and also it can be coupled with other rapid flow models under some simplifications (Tahmasebi and Kamrava, 2018).

CRediT authorship contribution statement

Xiaoming Zhang: Methodology. **Pejman Tahmasebi:** Conceptualization, Supervision, Funding acquisition.

Declaration of Competing Interest

The authors declare that they have no known competing financial interests or personal relationships that could have appeared to influence the work reported in this paper.

Acknowledgements

This study was partially supported by NSF (Grant #CMMI-2000966), NIH (Grant # P20GM103432), and NASA (Grant #80NSSC19M0061).

References

- Adepu, M., Chen, S., Jiao, Y., Gel, A., Emady, H., 2021. Wall to particle bed contact conduction heat transfer in a rotary drum using DEM. Comp. Part. Mech. 8 (3), 589–599
- Andrade, J.E., Lim, K.-W., Avila, C.F., Vlahinić, I., 2012. Granular element method for computational particle mechanics. Comput. Methods Appl. Mech. Eng. 241, 262–274. https://doi.org/10.1016/j.cma.2012.06.012.
- Anthony, J.L., Marone, C., 2005. Influence of particle characteristics on granular friction. J. Geophys. Res. 110, B08409. https://doi.org/10.1029/2004JB003399.
- Bailey, D.G., 2005. An Efficient Euclidean Distance Transform BT Combinatorial Image Analysis. In: Klette, R., Žunić, J. (Eds.), Springer. Berlin Heidelberg, Berlin, Heidelberg, pp. 394–408.
- Boon, C.W., Houlsby, G.T., Utili, S., 2012. A new algorithm for contact detection between convex polygonal and polyhedral particles in the discrete element method. Comput. Geotech. 44, 73–82. https://doi.org/10.1016/j.compgeo.2012.03.012.
- Buades, A., Coll, B., Morel, J.-M., 2005. A Non-Local Algorithm for Image Denoising, in: Proceedings of the 2005 IEEE Computer Society Conference on Computer Vision and Pattern Recognition (CVPR'05) - Volume 2 - Volume 02, CVPR '05. IEEE Computer Society, Washington, DC, USA, pp. 60–65. 10.1109/CVPR.2005.38.
- Chen, S., Adepu, M., Emady, H., Jiao, Y., Gel, A., 2017. Enhancing the physical modeling capability of open-source MFIX-DEM software for handling particle size polydispersity: implementation and validation. Powder Technol. 317, 117–125. https://doi.org/10.1016/J.POWTEC.2017.04.055.
- Cheng, H., Luding, S., Rivas, N., Harting, J., Magnanimo, V., 2019. Hydromicromechanical modeling of wave propagation in saturated granular crystals. Int. J. Numer. Anal. Methods Geomech. 43 (5), 1115–1139. https://doi.org/10.1002/nag.2920.
- Cho, G.-C., Dodds, J., Santamarina, J.C., 2006. Particle shape effects on packing density, stiffness, and strength: natural and crushed sands. J. Geotech. Geoenvironmental Eng. 132 (5), 591–602.
- Cundall, P.A., Strack, O.D.L., 1979. A discrete numerical model for granular assemblies. Géotechnique 29 (1), 47–65. https://doi.org/10.1680/geot.1979.29.1.47.
- Desrues, J., Viggiani, G., Bésuelle, P., 2010. Advances in X-ray Tomography for Geomaterials, Advances in X-ray Tomography for Geomaterials. Wiley-ISTE. 10.1002/9780470612187.
- Evans, D.J., Murad, S., 1977. Singularity free algorithm for molecular dynamics simulation of rigid polyatomics. Singularity free algorithm for molecular dynamics simulation of rigid polyatomics. 34 (2), 327–331.
- Felzenszwalb, P.F., Huttenlocher, D.P., 2012. Distance transforms of sampled functions. Theory Comput. 8 (1), 415–428.
- Ferellec, J.-F., McDowell, G.R., 2010. A method to model realistic particle shape and inertia in DEM. Granul. Matter 12 (5), 459–467. https://doi.org/10.1007/s10035-010-0205-8.
- Garcia, X., Latham, J.-P., Xiang, J., Harrison, J.P., 2009. A clustered overlapping sphere algorithm to represent real particles in discrete element modelling. Géotechnique 59 (9), 779–784. https://doi.org/10.1680/geot.8.T.037.
- Gedraite, E.S., Hadad, M., 2011. Investigation on the effect of a Gaussian Blur in image filtering and segmentation, in: Proceedings ELMAR-2011. pp. 393–396.

- Glowinski, R., Pan, T.W., Hesla, T.I., Joseph, D.D., Périaux, J., 2001. A fictitious domain approach to the direct numerical simulation of incompressible viscous flow past moving rigid bodies: application to particulate flow. J. Comput. Phys. 169 (2), 363–426. https://doi.org/10.1006/jcph.2000.6542.
- Goldstein, H., 2001. Classical Mechanics. Addison-Wesley, United States of America.
 Hager, A., 2014. CFD-DEM on Multiple Scales An Extensive Investigation of Particle-Fluid Interactions.
- Hager, A., Kloss, C., Pirker, S., Goniva, C., 2014. Parallel resolved open source CFD-DEM: Method, validation and application. J. Computat. Multiphase Flows. SAGE Publications Ltd STM 6 (1), 13–27. https://doi.org/10.1260/1757-482X.6.1.13.
- Hart, R., Cundall, P.A., Lemos, J., 1988. Formulation of a three-dimensional distinct element model—Part II. Mechanical calculations for motion and interaction of a system composed of many polyhedral. Int. J. Rock Mech. Min. Sci. Geomech. 25 https://doi.org/10.1016/0148-9062(88)92294-2.
- Hilton, J.E., Mason, L.R., Cleary, P.W., 2010. Dynamics of gas-solid fluidised beds with non-spherical particle geometry. Chem. Eng. Sci. 65 (5), 1584–1596. https://doi. org/10.1016/j.ces.2009.10.028.
- Hoomans, B.P.B., Kuipers, J.A.M., Briels, W.J., van Swaaij, W.P.M., 1996. Discrete particle simulation of bubble and slug formation in a two-dimensional gas-fluidised bed: A hard-sphere approach. Chem. Eng. Sci. 51 (1), 99–118. https://doi.org/ 10.1016/0009-2509(95)00271-5.
- Houlsby, G.T., 2009. Potential particles: a method for modelling non-circular particles in DEM. Comput. Geotech. 36 (6), 953–959. https://doi.org/10.1016/j. compgeo.2009.03.001.
- Huang, C.T., Mitchell, O.R., 1994. A Euclidean distance transform using grayscale morphology decomposition. IEEE Trans. Pattern Anal. Mach. Intell. 16, 443–448. https://doi.org/10.1109/34.277600.
- Jerves, A.X., Kawamoto, R.Y., Andrade, J.E., 2016. Effects of grain morphology on critical state: a computational analysis. Acta Geotech. 11 (3), 493–503. https://doi. org/10.1007/s11440-015-0422-8.
- Karimpouli, S., Tahmasebi, P., 2017. A hierarchical sampling for capturing permeability trend in rock physics. Transp. Porous Media 116 (3), 1057–1072. https://doi.org/ 10.1007/s11242-016-0812-x.
- Kawamoto, R., Andò, E., Viggiani, G., Andrade, J.E., 2016. Level set discrete element method for three-dimensional computations with triaxial case study. J. Mech. Phys. Solids 91, 1–13. https://doi.org/10.1016/j.jmps.2016.02.021.
- Kong, H., Akakin, H.C., Sarma, S.E., 2013. A generalized Laplacian of Gaussian filter for blob detection and its applications. IEEE Trans. Cybern. 43 (6), 1719–1733. https:// doi.org/10.1109/TSMCB.2012.2228639.
- Krumbein, W.C., 1941. Measurement and geological significance of shape and roundness of sedimentary particles. J. Sediment. Res. 11, 64–72. https://doi.org/10.1306/ D42690F3-2B26-11D7-8648000102C1865D.
- Laursen, T.A., 2013. Computational contact and impact mechanics: fundamentals of modeling interfacial phenomena in nonlinear finite element analysis. Springer Science & Business Media.
- Lim, K.-W., Andrade, J.E., 2014. Granular element method for three-dimensional discrete element calculations. Int. J. Numer. Anal. Methods Geomech. 38 (2), 167–188. https://doi.org/10.1002/nag.2203.
- Lim, K.-W., Krabbenhoft, K., Andrade, J.E., 2014. On the contact treatment of nonconvex particles in the granular element method. Comput. Part. Mech. 1 (3), 257–275. https://doi.org/10.1007/s40571-014-0019-2.
- Mair, K., Frye, K.M., Marone, C., 2002. Influence of grain characteristics on the friction of granular shear zones: GRAIN SHAPE INFLUENCE ON FRICTION. J. Geophys. Res. 107 (B10), ECV 4-1–ECV 4-9.
- Murphy, K.A., Dahmen, K.A., Jaeger, H.M., 2019. Transforming mesoscale granular plasticity through particle shape. Phys. Rev. X 9, 11014. https://doi.org/10.1103/ PhysRevX.9.011014.
- Patankar, N.A., Singh, P., Joseph, D.D., Glowinski, R., Pan, T.-W., 2000. A new formulation of the distributed Lagrange multiplier/fictitious domain method for particulate flows. Int. J. Multiph. Flow 26 (9), 1509–1524. https://doi.org/10.1016/ \$0301-9322(99)00100-7.
- Peña, A.A., Lind, P.G., Herrmann, H.J., 2008. Modeling slow deformation of polygonal particles using DEM. Particuology 6 (6), 506–514.
- Powers, M.C., 1953. A new roundness scale for sedimentary particles. J. Sediment. Res. 23, 117–119. https://doi.org/10.1306/D4269567-2B26-11D7-8648000102C1865D.
- Ren, B., Zhong, W., Chen, Y.u., Chen, X.i., Jin, B., Yuan, Z., Lu, Y., 2012. CFD-DEM simulation of spouting of corn-shaped particles. Particuology 10 (5), 562–572. https://doi.org/10.1016/j.partic.2012.03.011.
- Robinson, M., Ramaioli, M., Luding, S., 2014. Fluid–particle flow simulations using two-way-coupled mesoscale SPH–DEM and validation. Int. J. Multiph. Flow 59, 121–134. https://doi.org/10.1016/j.ijmultiphaseflow.2013.11.003.
- Saadatfar, M., Sheppard, A.P., Senden, T.J., Kabla, A.J., 2012. Mapping forces in a 3D elastic assembly of grains. J. Mech. Phys. Solids 60 (1), 55–66. https://doi.org/10.1016/j.jmps.2011.10.001.
- Seyedi Hosseininia, E., Mirghasemi, A.A., 2006. Numerical simulation of breakage of two-dimensional polygon-shaped particles using discrete element method. Powder Technol. 166 (2), 100–112. https://doi.org/10.1016/j.powtec.2006.05.006.
- Shirgaonkar, A.A., MacIver, M.A., Patankar, N.A., 2009. A new mathematical formulation and fast algorithm for fully resolved simulation of self-propulsion. J. Comput. Phys. 228 (7), 2366–2390. https://doi.org/10.1016/j.jcp.2008.12.006.
- Tahmasebi, P., 2018a. Accurate modeling and evaluation of microstructures in complex materials. Phys. Rev. E 97, 023307. https://doi.org/10.1103/PhysRevE.97.023307.
- Tahmasebi, P., 2018b. Packing of discrete and irregular particles. Comput. Geotech. 100, 52–61.

- Tahmasebi, P., Kamrava, S., 2019. A pore-scale mathematical modeling of fluid-particle interactions: Thermo-hydro-mechanical coupling. Int. J. Greenh. Gas Control. 83, 245–255. https://doi.org/10.1016/j.ijggc.2018.12.014.
- Tahmasebi, P., Kamrava, S., 2018. Rapid multiscale modeling of flow in porous media. Phys. Rev. E 98, 052901. https://doi.org/10.1103/PhysRevE.98.052901.
- Tomac, I., Gutierrez, M., 2014. Fluid lubrication effects on particle flow and transport in a channel. Int. J. Multiph. Flow 65, 143–156. https://doi.org/10.1016/j. ijmultiphaseflow.2014.04.007.
- Tomac, I., Gutierrez, M., 2013. Discrete element modeling of non-linear submerged particle collisions. Granul. Matter 15 (6), 759–769. https://doi.org/10.1007/ s10035-013-0442-8.
- Topin, V., Monerie, Y., Perales, F., Radjaï, F., 2012. Collapse dynamics and runout of dense granular materials in a fluid. Phys. Rev. Lett. 109, 188001 https://doi.org/ 10.1103/PhysRevLett.109.188001.
- Tsuji, T., Yabumoto, K., Tanaka, T., 2008. Spontaneous structures in three-dimensional bubbling gas-fluidized bed by parallel DEM-CFD coupling simulation. Powder Technol. 184 (2), 132–140. https://doi.org/10.1016/j.powtec.2007.11.042.
- Tsuji, Y., Tanaka, T., Ishida, T., 1992. Lagrangian numerical simulation of plug flow of cohesionless particles in a horizontal pipe. Powder Technol. 71 (3), 239–250. https://doi.org/10.1016/0032-5910(92)88030-L.
- Wadell, H., 1932. Volume, shape, and roundness of rock particles. J. Geol. 40 (5), 443–451. https://doi.org/10.1086/623964.
- Walton, O.R., Braun, R.L., 1993. Simulation of rotary-drum and repose tests for frictional spheres and rigid sphere clusters.

- Xu, B.H., Yu, A.B., 1997. Numerical simulation of the gas-solid flow in a fluidized bed by combining discrete particle method with computational fluid dynamics. Chem. Eng. Sci. 52 (16), 2785–2809. https://doi.org/10.1016/S0009-2509(97)00081-X.
- Zhang, X., Tahmasebi, P., 2019. Effects of grain size on deformation in porous media. Transp. Porous Media 129 (1), 321–341. https://doi.org/10.1007/s11242-019-01291-1
- Zhang, X., Tahmasebi, P., 2018. Micromechanical evaluation of rock and fluid interactions. Int. J. Greenh. Gas Control 76, 266–277. https://doi.org/10.1016/J. LJGGC.2018.07.018.
- Zhao, J., Shan, T., 2013. Coupled CFD–DEM simulation of fluid–particle interaction in geomechanics. Powder Technol. 239, 248–258. https://doi.org/10.1016/j. powtec.2013.02.003.
- Zhao, T., Utili, S., Crosta, G.B., 2016. Rockslide and Impulse Wave Modelling in the Vajont Reservoir by DEM-CFD Analyses. Rock Mech. Rock Eng. 49 (6), 2437–2456. https://doi.org/10.1007/s00603-015-0731-0.
- Zhong, W.-Q., Zhang, Y., Jin, B.-S., Zhang, M.-Y., 2009. Discrete Element Method Simulation of Cylinder-Shaped Particle Flow in a Gas-Solid Fluidized Bed. Chem. Eng. Technol. 32, 386–391. https://doi.org/10.1002/ceat.200800516.
- Zhong, W., Yu, A., Liu, X., Tong, Z., Zhang, H., 2016. DEM/CFD-DEM modelling of non-spherical particulate systems: theoretical developments and applications. Powder Technol. 302, 108–152.
- Zhu, H.P., Zhou, Z.Y., Yang, R.Y., Yu, A.B., 2008. Discrete particle simulation of particulate systems: a review of major applications and findings. Chem. Eng. Sci. 63 (23), 5728–5770.
- Zhu, H.P., Zhou, Z.Y., Yang, R.Y., Yu, A.B., 2007. Discrete particle simulation of particulate systems: theoretical developments. Chem. Eng. Sci. 62 (13), 3378–3396.